Drag reduction on a three-dimensional blunt body with different rear cavities under cross-wind conditions

M. Lorite-Díez[a], J.I. Jiménez-González[a,*], L. Pastur[b], O. Cadot[c], C. Martínez-Bazán[a]

[a] *Departamento de Ingeniería Mecánica y Minera. Universidad de Jaén. Campus de las Lagunillas, 23071, Jaén, Spain.*
[b] *IMSIA-ENSTA ParisTech, 828 Bd des Maréchaux F-91762 Palaiseau, France.*
[c] *School of Engineering, University of Liverpool, Liverpool L69 3GH, UK.*

Abstract

The use of rear cavities at the base of a square-back Ahmed body has been experimentally evaluated as a passive control device under cross-wind conditions with yaw angles $\beta \leq 10^o$, by means of pressure, force and velocity measurements. A comparative study has been performed at a Reynolds number $Re = 10^5$, considering the reference square-back body (i.e. the body without any passive control device), and the same body implementing both straight and curved cavities as add-on devices. It is shown that the performance of a straight cavity, which is widely acknowledged as a robust drag reduction device for car models, is hindered under moderate cross-wind conditions, and does not constitute an efficient control strategy, especially when compared with a curved cavity.

In particular, when the freestream is aligned with the body, the curved cavity provides a stronger attenuation of the fluctuating nature and the bi-stable dynamics of the wake (characteristic of the wake behind a square-back Ahmed body) than the straight one. Besides, the reduced size of the near wake, which is provoked by flow re-orientation and the reduced span between the rear edges of the curved cavity, leads to an important base pressure recovery, that translates into relative reductions of the drag of 9.1% in comparison with the reference case (i.e. 2.6%, with respect to the straight cavity). The results are considerably improved under cross-wind conditions, since the increase with the yaw angle of the force is particularly intense for the body with the straight cavity and attenuated for the model with the curved cavity. Thus, the relative reduction of the drag coefficient with respect to the reference body becomes negligible for the straight device at a yaw angle of 10^o, while it still represents approximately a 10% for the curved cavity. Furthermore, flow visualizations show that the wake is deflected as the incident flow is increasingly yawed, leading to the formation of a single leeward vortex core that approaches progressively the body, decreasing the base pressure. This phenomenon is minored when a curved cavity is implemented, increasing the low pressure induced at the body base.

1. Introduction

Road transportation represents approximately 70% of the global transport industry (see e.g. Acker, 2018), and its energy consumption and environmental impact have become major social concerns in the last decades. An important part of the associated energy expenses are due to aerodynamic loads. In that regard, Choi et al. (2014) state that at least a 21% of trailer's fuel total consumption (driving at 105 km/h), is related to aerodynamic drag, which increases quadratically with the relative vehicle velocity. Consequently, road transportation constitutes a major source of emissions of greenhouse effect gases, such as CO_2, due to the large fuel consumption needed, in part, to overcome aerodynamics loads. This justifies the intense research work devoted to develop strategies of flow control and drag reduction in heavy vehicles, aiming at reducing the environmental impact (see e.g. Hucho and Sovran, 1993; Choi et al., 2014, and references therein).

The bluff geometry of heavy ground vehicles, especially conceived to maximize the transportation capacity and simplify the loading process in docks, entails the flow separation at the rear end, thus leading to the

*Corresponding author
Email address: `jignacio@ujaen.es` (J.I. Jiménez-González)

generation of a turbulent wake, which is responsible for the limited vehicle aerodynamic performance. In particular, it is estimated that, in this type of vehicles, approximately 25% of the aerodynamic drag resistance is connected to the rear end (Wood and Bauer, 2003). Consequently, most of the flow control strategies developed over the past years, have been mainly designed to act on the flow separation at the back edge of the vehicle and the near-wake region. Besides, the complexity of the flow around heavy vehicles has led to the establishment of simplified vehicle models, which retain most of the features of the wake of heavy vehicles. Classical examples of three-dimensional bluff models with rounded fore-body are the one proposed by Ahmed et al. (1984), which is characterized by a slanted rear surface, and the corresponding square-back version used by Han et al. (1996).

Interestingly, such square-back bodies are known to exhibit an unsteady vortex shedding from the shear layers, together with a bi-stable random dynamics characterized by the intermittent switching between two horizontally deflected mirror positions (Grandemange et al., 2013b,a), whose origin stems from the destabilization of steady Reflectional Symmetry Breaking, RSB, modes at the laminar flow (Grandemange et al., 2012). The presence of these RSB modes also produces additional lateral loads on the body. Therefore, a good control should also attempt to suppress the permanent wake asymmetry by stabilizing the RSB mode toward the symmetry preserved wake.

Among the different rear flow control strategies that have been proposed in the literature, rear cavities or flaps (see e.g. Sanmiguel-Rojas et al., 2011; Martín-Alcántara et al., 2014; Evrard et al., 2016; Brackston et al., 2016) stand out as efficient passive devices in terms of wake pressure recovery, drag reduction and attenuation of vortex shedding. In particular, their efficiency highly depends on the cavity or flap depth, what may represent a limitation in practical applications where size restrictions exist for add-on devices (as occurs with European legislation for heavy transport weight and dimensions). Thus, shape optimization techniques based on adjoint sensitivity analyses (Meliga et al., 2014; Othmer, 2014) constitute relevant design tools to improve the performance of these passive devices. Such approach has been recently employed by Lorite-Díez et al. (2017), where a curved rear cavity was designed, for a two-dimensional D-shaped body, after shape optimization of a straight cavity with a depth of $0.3h$, being h the body's height. The curved cavity was shown to reduce the drag coefficient by 30% with respect to the straight cavity configuration under permanent turbulent flow regimes, i.e. Reynolds number of 20,000. Similar results were later obtained for transient flow conditions, by analyzing experimentally the starting wake created by a body that accelerates from rest (Lorite-Díez et al., 2018). However, the performance of such curved cavity still needs to be investigated on a square-back Ahmed-like model under more realistic turbulent conditions.

On the other hand, the presence of side wind can significantly alter the flow detachment and the near wake properties, thus leading to the increase of side and drag forces, and the vehicle's instability (Hucho and Sovran, 1993). On average, road vehicles operate most of the time at wind conditions which are not aligned with the road and, therefore, it is usual to evaluate forces and flow features of simplified heavy vehicle models over wide ranges of the yaw angle, β, which accounts for the misalignment of the model with respect to the incident freestream. In particular, typical studies of cross-wind are focused on the range given by $\beta = \pm 10^{\text{o}}$, which are representative limits of the yaw angle for typical driving conditions (Gardell, 1980; Hucho and Sovran, 1993; D'Hooge et al., 2014), and are in line with the new requirements for vehicles testing in the European Union. Variations of force coefficients within such region are characterized by important monotonic growths with the yaw angle, as shown by Bello-Millán et al. (2016) for a 25^{o} back-slanted Ahmed body in the range of $\beta \leq 60^{\text{o}}$. In addition to the increase of the frontal apparent area as the value of β grows, the growth in drag coefficient is also associated with the development of streamwise vortices along the vehicle's length and rear bottom of the base (Rao et al., 2018), which may interact with the original streamwise $C - pillar$ vortices, to create a near-wake toroidal vortical structure (Hassaan et al., 2018), thus leading to lower values of pressure in the near wake region (McArthur et al., 2018). Therefore, a complete analysis of the performance of passive control devices requires the evaluation of flow features and force coefficients for different values of the yaw angle (as e.g. in Grandemange et al., 2015; Hassaan et al., 2018).

However, the number of studies dealing with wake control under yawed conditions is still small (see e.g. García de la Cruz et al., 2017; Li et al., 2019) in comparison with those focusing on aligned conditions. In particular, to the best of our knowledge, little research has been performed on the effect of rear cavities for the control of road vehicles under cross-flow condition, an exception being the work by Bonnavion and Cadot (2018), where the straight cavity was tested for very low yaw angles ($|\beta| \leq 2$). Their results show that the performance of a cavity (created by moving the base inwards, keeping constant the total vehicle's length) is

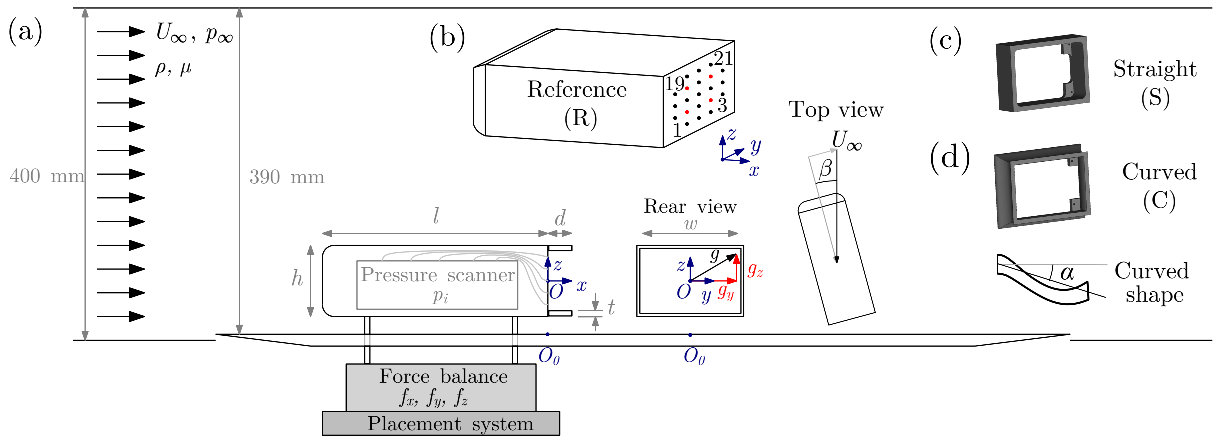

Figure 1: (a) Sketch of the experimental set-up, along with rear and top views of the model. (b) Pressure taps distribution at the base of reference (R) configuration. (c, d) Rear passive devices, including the (c) straight cavity (S) and the (d) curved cavity (C) with its corresponding profile shape.

hindered in terms of force and pressure coefficients as the yaw grows. Thus, we wonder if the curved cavity is a more appropriate wake control system under cross-wind conditions.

The present work aims at investigating experimentally the performance of rear cavities of different geometries at yawed conditions. First, the limitations of a straight cavity, when implemented as an add-on device (as in real applications), over a wide range of yaw angles, will be evaluated. Secondly, the performance of a curved cavity, whose profile has been obtained by shape optimization in Lorite-Díez et al. (2017), will also be studied, determining thus the suitability of simplified two-dimensional adjoint optimization approaches to design efficient flow control strategies devices in more realistic flow conditions.

Thus, the paper is organized as follows: the problem definition and experimental details are introduced in Sect. 2. Next, Sect. 3 is devoted to analyze the results, comparing force, pressure and velocity measurements obtained with the different configurations. In particular, we first describe in Sect. 3.1 the main flow features, while the effect of cross-wind conditions and the yaw angle is presented in Sect. 3.2. Finally, the main conclusions are drawn in Sect. 4.

2. Problem description and experimental details

2.1. Problem description

We investigate experimentally the flow around a square-back Ahmed-like body of length $l = 261$ mm, width $w = 97.25$ mm and height $h = 72$ mm. The model is placed inside an Eiffel-type wind tunnel of 390 mm $\times$ 390 mm test section (see Fig. 1a), using a rotatory positioning system which allows to modify the yaw angle β of the body (see top view at Fig. 1a) with an accuracy of $0.01°$. In order to have constant flow conditions, a ground plate is placed at 10 mm above the lower face of the inlet and triggers the turbulent boundary layer 140 mm upstream of the forebody without separation at the leading edge. Four holding rods of 7.5 mm diameter ($0.104\,h$) are used to support the model with a ground clearance of $c/h = 0.278$. Two different passive control devices, i.e a straight and a curved cavity of depth $d/h = 0.3$ and thickness $t/h = 0.05$ (Figs. 1c,d), are implemented at the rear of the reference model to evaluate their effect on the turbulent wake behind the body. In particular, the curved cavity, which presents a slant angle $\alpha = 12.5°$, represents a three-dimensional adaptation of the rear device obtained by means of adjoint sensitivity and shape optimization approaches by Lorite-Díez et al. (2017) (see Fig. 1d). The performance of both, the curved (C model) and straight cavities (S model), as drag reduction and wake control devices, will be analyzed by adding them to the reference square-back model (R model) of original length $l/h = 3.625$, thus leading to an extended length of $l + d = 3.925\,h$. Notice that such a set-up is thought to reproduce qualitatively the geometrical conditions in real heavy vehicles applications, where add-on devices are appended to the basic geometry of trucks (which usually present larger aspect ratios l/h).

The wind tunnel was set to generate a uniform freestream velocity of $U_\infty = 20$ m/s, with a turbulent intensity below 0.5% and a velocity homogeneity over the test section better than 0.3% (further details as the incoming velocity profile shape can be found in Grandemange et al., 2013b). The Reynolds number based on the height of the model h was $Re = \rho U_\infty h/\mu \simeq 10^5$, where ρ and μ are respectively the density and viscosity of air. Besides, the effect of crosswind was investigated by varying the yaw angle β, i.e. the incoming flow angle (see Fig. 1a), within the range of $0 \leq \beta \leq 10°$, with increments of $\Delta\beta = 1°$.

Two Cartesian coordinates systems were used in the present study: a local body-based system and a global system, referred to the wind-tunnel. The origin O of the body-based coordinates system (x, y, z) was located at the center of the body base, with x being the direction aligned with the longitudinal body axis, z the vertical direction, and y the side direction that forms a direct trihedral. The velocity vector can be then decomposed into these directions, being their components $\mathbf{u} = (u_x, u_y, u_z)$. On the other hand, the global coordinates will denoted as (x_0, y_0, z_0), with x_0 being parallel to the free-stream and the origin, O_0, placed at the ground, as shown in Fig. 1.

2.2. Pressure, force and velocity measurements

Pressure measurements were performed at the base of the reference body using 21 pressure taps distributed along a structured, equispaced grid with $\Delta y = 19$ mm and $\Delta z = 13$ mm, as displayed in Fig. 1(b). Pressure values, p_i ($i = 1, 2, \ldots, 21$), were acquired with a Scanivalve ZOC22B/32 5″ H_2O pressure scanner and a gle/SmartZOC-100 acquisition and control unit (accuracy of 3.75 Pa), using a sampling frequency of 50 Hz per channel, during 250 s for typical experiments. Such conditions have been proven to be good enough to resolve the main wake properties and the bi-stable dynamics. Moreover, the static pressure value, p_∞, was measured far upstream from the model at the inlet of the test section. The pressure taps were connected through vinyl tubes to the pressure scanner, which was placed inside the model to limit the length of the tubes and the associated filtering effect. Base pressure measurements will be expressed in terms of the dimensionless pressure coefficient as

$$c_{p,i}(y, z, t) = \frac{p_i(y, z, t) - p_\infty}{\rho U_\infty^2/2}. \tag{1}$$

The uncertainty of the pressure coefficient is approximately ± 0.002. These measurements will evaluate instantaneously the suction coefficient (Roshko, 1993) of the blunt base area, given by

$$c_B = -\frac{1}{n}\Sigma_{i=1}^{n} c_{p,i}(y_i, z_i, t), \tag{2}$$

where $n = 21$ is the total number of base pressure taps.

Besides, the wake asymmetry can be quantified through the horizontal and vertical pressure gradients, i.e. g_y and g_z respectively, calculated using the measurements from the four pressure taps highlighted in red in Fig. 1(b), namely taps $i = 5, 7, 15, 17$; as done in (Grandemange et al., 2013a; Lorite-Díez et al., 2019). Such pressure gradients are computed as

$$g_y = \frac{\partial c_p}{\partial y} \simeq \frac{1}{2}\left[\frac{c_p(y_{17}, z_{17}, t) - c_p(y_{15}, z_{15}, t)}{y_{17} - y_{15}} + \frac{c_p(y_7, z_7, t) - c_p(y_5, z_5, t)}{y_7 - y_5}\right], \tag{3}$$

$$g_z = \frac{\partial c_p}{\partial z} \simeq \frac{1}{2}\left[\frac{c_p(y_{15}, z_{15}, t) - c_p(y_5, z_5, t)}{z_{15} - z_5} + \frac{c_p(y_{17}, z_{17}, t) - c_p(y_7, z_7, t)}{z_{17} - z_7}\right]. \tag{4}$$

Note that the statistical evaluation of the value of g_y will allow to characterize the occurrence of the two asymmetric RSB modes identified by Grandemange et al. (2013b). Thus, a positive RSB state (P state) will be present at the wake when $g_y > 0$, while the negative RSB state (N state) will exist for $g_y < 0$. Also, as depicted at the rear view in Fig. 1(a), both horizontal and vertical pressure gradients are components of an asymmetry gradient vector (Bonnavion and Cadot, 2018) whose modulus, g, is computed as $g = \sqrt{g_y^2 + g_z^2}$. Therefore, the value of g will be used to quantify the strength of the global asymmetry of the wake.

Moreover, the aerodynamic forces were also obtained for all geometries and body orientations with the use of a multi-axial load cell (model AMTI-MC3A-100lb) which was connected to the model through the four cylindrical supports, allowing to measure the instantaneous forces along the coordinate axes, i.e. the drag force f_x, the side force f_y and the lift force f_z. Such force signals were recorded during 30 s at a sampling rate of 1 kHz. The measurements uncertainty was estimated (using specifications of crosstalk, non-linearity and hysteresis) to be below 0.002 N for the x and y directions and below 0.006 N for the z direction. Since the load cell and the model were jointly installed on top of the positioning system (Fig. 1), they rotate together as the turntable moves to set the yaw angle β of interest. Therefore, forces on the x and y axes are combined to obtain the drag force f_{x0} in the wind direction, or global coordinate x_0, as

$$f_{x0} = f_x \cdot \cos\beta + f_y \cdot \sin\beta. \tag{5}$$

The dimensionless force coefficients were defined as

$$c_i = \frac{f_i}{\rho U_\infty^2 hw/2}, \tag{6}$$

where the base area hw was used as reference, with an accuracy of ± 0.001 for c_x, c_y or c_d, and ± 0.003 for c_z. Note that the maximum blockage ratio, corresponding to $\beta = 10^\circ$, was 6.68 % (computed using the corrected projected area under cross-wind). Thus, considering that the test section was not enclosed by lateral walls and therefore, the flow did not accelerate due to blockage effects, no further corrections have been required to determine the forces acting on the body from the balance.

Additionally, the spatial characterization of the near wake was obtained by means of Particle Image Velocimetry (PIV) measurements, at two different horizontal planes located at $z = 0$ to obtain the velocity fields $\mathbf{u_{xy}} = (u_x, u_y, 0)$, in order to observe the main features of the recirculating region.

The PIV system used a dual pulse laser (Nd:YAG, 2 x 135mJ, 4ns) synchronized with a FlowSense EO, 4 Mpx, CCD camera. The laser sheet was pulsed with time delays of 50μs, and the set-up acquired 500 pairs of images at 10 Hz, ensuring a good resolution in terms of the number of images to properly obtain the velocity averaged fields. Besides, to ensure the repeatability and the accuracy of the results, three different PIV tests were run for each experiment. The interrogation window was set to 16 $\times$ 16 pixels with an overlap of 50%, resulting into a spatial grid of 222 $\times$ 295 points, whose resolution is approximately 1% of body's height. More details about the PIV procedure can be found in Lorite-Díez et al. (2019).

To complement the PIV velocity measurements, local measurements of the streamwise velocity, $u_x(t)$, were performed with a hot wire sensor (wire of 5μm diameter and 1.25 mm length) placed at $P_{\text{hwa}}(x, y, z) = (2.5h, 0, 0.35h)$, aiming at characterizing, with a good temporal resolution, the wake fluctuations associated with the vortex shedding process. Such tests were performed with a sampling frequency of 1 kHz during 120 s. To identify the dominant angular frequencies at the wake, ϖ, power spectral density distributions (PSD) were used, with a sliding averaging window of 2 s. Values of frequencies can be expressed in non-dimensional form, as Strouhal numbers

$$St = \frac{\varpi h}{2\pi U_\infty}. \tag{7}$$

Finally, note that, as indicated above, conditional statistic will be performed to identify the RSB positive (P) and negative (N) states of the wake, by evaluating the value of the horizontal pressure gradient, g_y. Thus, since pressure and PIV measurements were simultaneously recorded, an appropriate conditional averaging on the velocity fields can be performed to capture the wake topology corresponding to P and N states. In the following, the results will be expressed in dimensionless variables, using h, U_∞, $0.5\rho U_\infty^2$ and h/U_∞ as characteristic length, velocity, pressure, and time scales, respectively. Besides, the time-averaged of any instantaneous variable $a(x, y, z, t)$, will be denoted as $A = \overline{a}$, whereas its corresponding standard deviation, employed to evaluate the amplitude of the fluctuations, $a' = a - A$, will be expressed as $A' = \sqrt{\overline{(a')^2}}$. Also, we will denote by a superscript P or N the conditional averaging of any variables related to the deflected P or N states. Additionally, relative values with respect to the reference geometry, R, will be expressed with Δ, as $\Delta_A^i = (A^i - A^{\mathrm{R}})/A^{\mathrm{R}}$.

3. Results

We next describe the main results obtained from the force, pressure and velocity measurements for the three configurations, i.e. the reference square-back model (R), and the models with straight (S) and curved (C) rear cavities, respectively. First, the main flow features will be analyzed for aligned flow conditions ($\beta = 0^\circ$) in Sect. 3.1, while the effect of cross-wind on the main flow variables are subsequently described in Sect. 3.2.

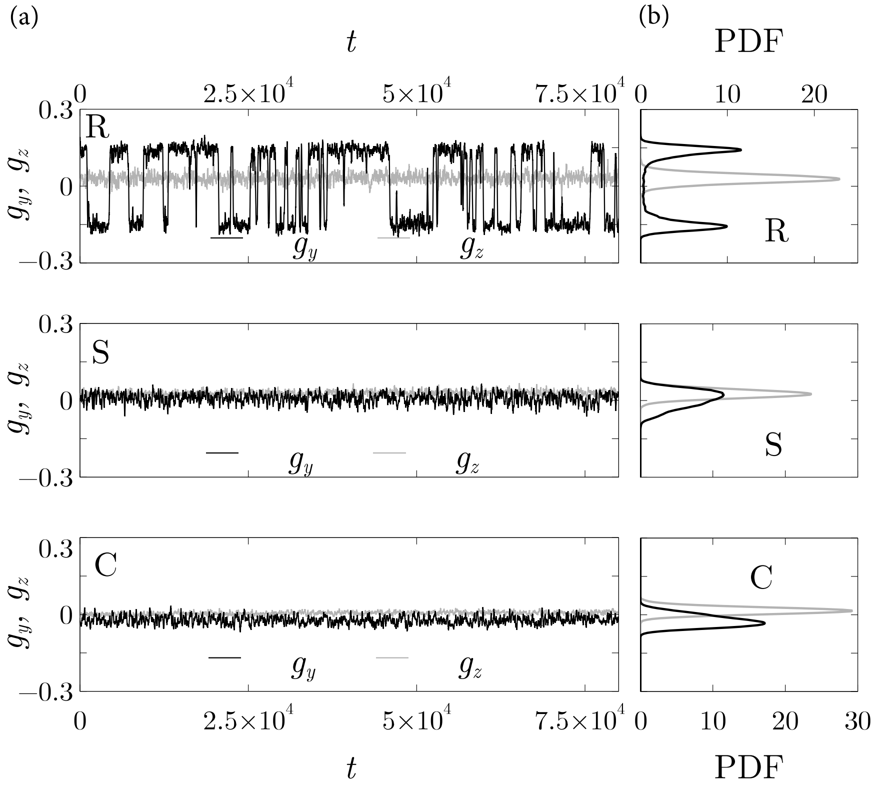

Figure 2: (a) Time evolution of the horizontal, g_y (black lines), and the vertical, g_z (grey lines), base pressure gradients for all configurations (reference case, R - top row, straight cavity, S - middle row, and curved cavity, C - bottom row) and (b) corresponding Probability Density Functions (PDF).

3.1. Flow features for $\beta = 0°$

It is known that the wake behind the reference square-back model sustains a long-time bi-stable dynamics, characterized by the intermittent switching between two horizontally deflected RSB states (Grandemange et al., 2013b). Such bi-stable behavior in the $y-$axis is clearly identified by the random changes from positive (negative) to negative (positive) values of the horizontal base pressure gradient, g_y, shown in Fig. 2(a). The corresponding probability density function (PDF) in Fig. 2(b) shows that the wake exhibits, with the same probability, two mirrored states, denoted P and N.

On the other hand, the vertical base pressure gradient, g_z, remains nearly constant, with a mean value given by $G_z^{\mathrm{R}} = 0.031$. The total wake asymmetry can be then quantified by $g(t) = \sqrt{g_y^2 + g_z^2}$, which for the reference case yields a mean value of $G^{\mathrm{R}} = 0.142$. As reported by Evrard et al. (2016), the addition of a straight cavity of depth $d \gtrsim 0.25$, leads to the symmetrization of the base pressure distribution, suppressing the RSB modes and consequently, the bi-stable dynamics. Such outcome is clearly observed in Fig. 2(a), where now the horizontal pressure gradient remains constant and close to zero, with $G_y^{\mathrm{S}} = 0.033$, and is characterized by a single peak in the corresponding PDF (Fig. 2b). Consequently, the magnitude of the total pressure gradient, $G^{\mathrm{S}} = 0.046$, is considerably smaller than that reported for the reference case, despite the fact that the vertical pressure gradient, $G_z^{\mathrm{S}} = 0.026$, is barely affected. The base pressure distribution is almost symmetric as well when the curved cavity is used according to Fig. 2(a), resulting in a small horizontal base gradient, $G_y^{\mathrm{C}} = -0.022$. Moreover, the amplitudes of the fluctuations of g_y and g_z are even smaller than those in the straight cavity and the reference cases, giving $G_z^{\mathrm{C}} = 0.017 < G_z^{\mathrm{S}}$, what leads to a smaller magnitude of the total base pressure gradient, $G^{\mathrm{C}} = 0.035$.

The near wake topologies of the different configurations are depicted in Fig 3(a), where the time-averaged contours of streamwise velocity U_x and flow streamlines at the plane $z = 0$ are displayed. The conditional averaged asymmetric P state is shown in Fig 3(a) for the reference case, with the recirculating bubble displaying

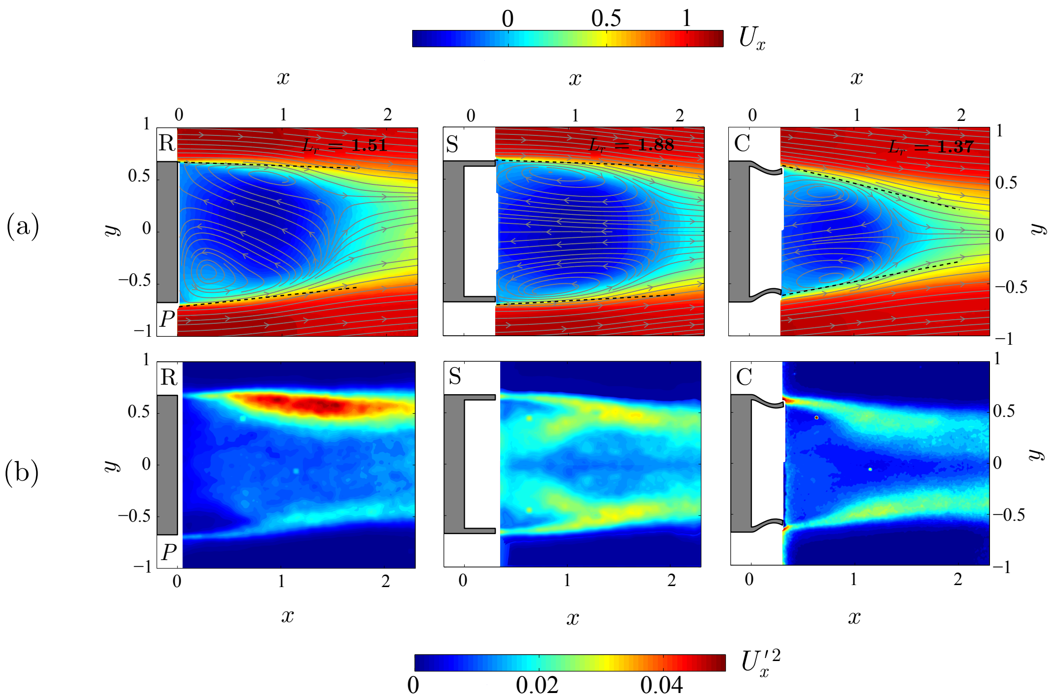

Figure 3: Time-averaged near wake topology for the reference case (R), straight (S) and curved cavities (C) in $z = 0$ plane: (a) streamwise velocity contours along with flow streamlines, and (b) streamwise Reynolds stresses. For the R case, only the conditionally averaged P state is shown. Black dashed lines in (a) illustrate the separation angle.

two asymmetric cores, which deflect the backflow towards the $y > 0$ region, leading to a positive value of g_y at the base.

As expected, with the use of a straight cavity, the near wake displays an almost symmetric wake topology and an increase in the length of the recirculating bubble. In contrast, the symmetric recirculation region becomes considerably smaller and thinner when the curved cavity is used instead, due to the modification of the separation angle introduced by the slanted geometry.

Furthermore, the wake fluctuations are also shown in Fig. 3(b) through averaged contours of the streamwise Reynolds stresses, $U_x'^2$. For the reference case, the P state shows strong fluctuations in the adverse velocity region of the wake, as in Grandemange et al. (2013b). The addition of rear cavities leads to the reduction of the fluctuations along the shear layers, being it particularly relevant for the curved configuration, where the shear layers are also thickened due to the flow re-orientation at separation (the induced separation angle by the curved geometry is 12.5°).

For the sake of clarity, a comparison of the mean values of the aforementioned main global flow variables is provided in Table 1 for the three bodies under consideration. In particular, values of the horizontal, vertical and total base pressure gradients, G_y, G_z and G, are given, together with the length of the recirculating bubble, L_r. Notice that the implementation of the curved cavity provides a reduction of $\Delta_G^{\mathrm{C}} = -82.4\%$ in the magnitude of the total pressure gradient, G, with respect to the reference square-back model. Such value represents an additional reduction of 14.8% when compared to the straight cavity, $\Delta_G^{\mathrm{S}} = -67.6\%$. Therefore, it constitutes a more efficient device in terms of wake symmetrization (note that a similar mitigation of the wake bi-stable dynamics was also achieved through base flaps for a truck-like model by Schmidt et al., 2018). Table 1 also lists values of the suction coefficient, C_B, and the drag coefficient, C_x, and their respective relative variations, which will be subsequently discussed. It should be recalled that C_B refers to the mean pressure over the blunt trailing edge that exactly corresponds to the base drag of the reference model, and to the suction at the bottom for both S and C cavities. The evaluation of the base drag of both models with cavity would have implied the measurements of the pressure all over the extension that is not performed here.

Let us now describe Fig. 4, which depicts contours of the time-averaged and RMS base pressure, $C_p(y, z)$

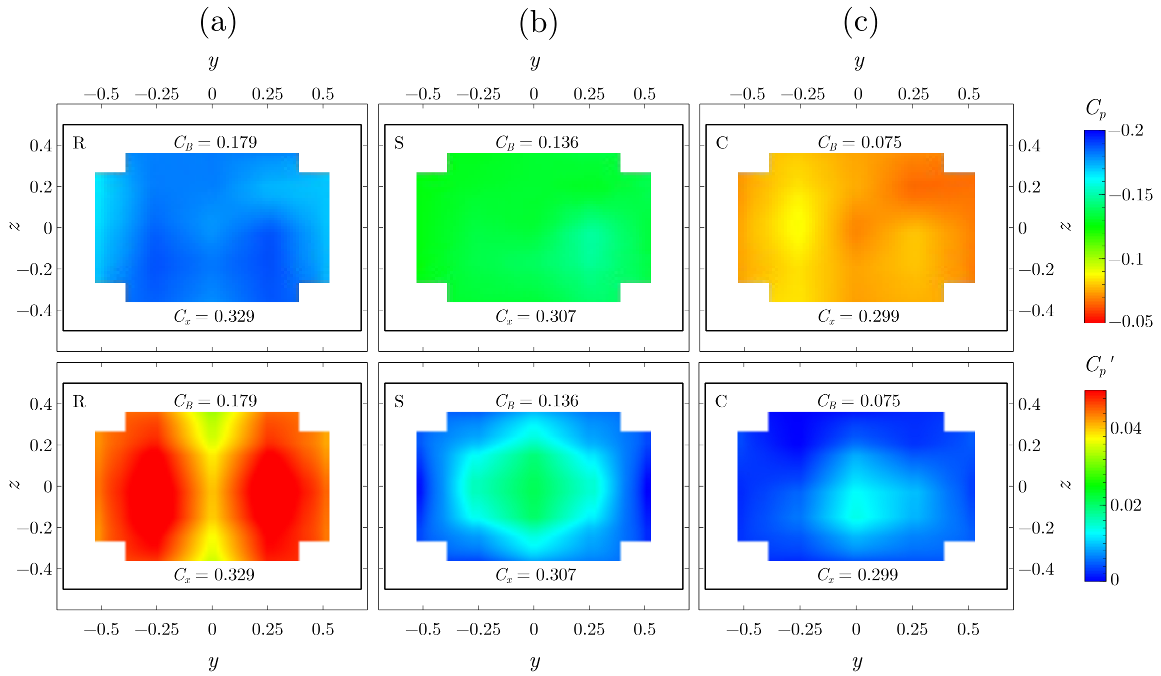

Figure 4: Averaged base pressure distribution $C_p(y,z)$ and RMS base pressure topology $C'_p(y,z)$ along with values of suction, C_B, and drag coefficients, C_x, for the three configurations under study: (a) reference case (R), (b) straight (S) and (c) curved (C) cavities.

and $C'_p(y,z)$, respectively, measured at the blunt surface of the square-back model ($x=0$), for the reference case in Fig. 4(a), the model with straight cavity in Fig. 4(b) and the model with the curved cavity in Fig. 4(c). In particular, the reference case displays a nearly symmetric averaged distribution (on account of the contributions of both equally probable P and N asymmetric states), being both deflected wake locations clearly distinguished in the RMS distribution. Both states are characterized by low values of C_p and high amplitudes of C'_p in Fig. 4(a). Thus, the suction coefficient stemming from the spatial averaging of such pressure distribution is $C_B^{\mathrm{R}} = 0.179$. Moreover, as detailed earlier, force measurements were also performed to obtain the mean drag coefficient, obtaining a value of $C_x^{\mathrm{R}} = 0.329$ for the reference square-back model. Thus, the base drag coefficient represents 54.4% of the mean drag coefficient C_x, which is similar to the contribution of the form drag for the Ahmed body reported by Ahmed et al. (1984) and Evrard et al. (2016). The addition of a rear straight cavity, and the subsequent suppression of the RSB mode, translates into a spatially uniform base pressure distribution with a reduced level of pressure fluctuations (see Fig. 4b) that yields a lower base drag coefficient of $C_B^{\mathrm{S}} = 0.136$, representing a 24.0% decrease with respect to the value C_B^{R}, as listed in Table 1. As shown in Table 1, the pressure recovery at the base is linked to an increase of L_r. In terms of forces, it translates into a 6.7% decrease of the mean drag coefficient value, $C_x^{\mathrm{S}} = 0.307$, with respect to the reference case.

The use of the curved cavity improves the base drag and the drag coefficients values with respect to the

#	G_y	G_z	G	L_r	C_B	C_x	$\Delta^i_G(\%)$	$\Delta^i_{C_B}(\%)$	$\Delta^i_{C_x}(\%)$
R	0.137 (P)	0.031	0.142	1.510	0.179	0.329	-	-	-
S	0.033	0.026	0.046	1.880	0.136	0.307	-67.6	-24.0	-6.7
C	-0.022	0.017	0.025	1.370	0.075	0.299	-82.4	-58.1	-9.1

Table 1: Mean values of main global flow characteristics for the reference model (R), model with straight (S) and curved (C) cavities: horizontal, vertical and total base pressure gradients, G_y, G_z and G; recirculating bubble length, L_r, suction coefficient, C_B, and drag coefficient, C_x. Note that the horizontal pressure gradient for the reference case corresponds to the conditional averaged value for the P state, G_y^P.

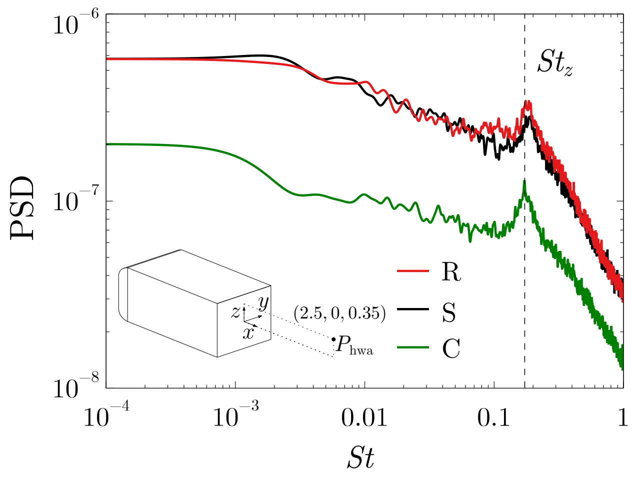

Figure 5: Power spectral density (PSD) of the streamwise velocity fluctuations, u'_x, measured at the location $(x, y, z) = (2.5, 0, 0.35)$ (see inset), for the three configurations under study.

straight one. In particular, as displayed in Fig. 4(c), the base pressure increases considerably, leading to a base drag coefficient of $C_B^{\rm C} = 0.075$, which is nearly half of that obtained with the straight cavity. In addition, the pressure fluctuations are also reduced. The associated drag coefficient yields $C_x^{\rm C} = 0.299$, which is a 9.1% lower than $C_x^{\rm R}$ corresponding to the reference model. Therefore, the curved cavity constitutes an improved control device with respect to a classical straight cavity, not only in terms of wake asymmetry, but also regarding the drag coefficient. Nevertheless, the reduction in C_x does not correspond with that of the suction C_B at the bottom of the cavity. This is a simple consequence of the pressure distribution on the cavity extension related to the outside flow curvature together with possible longitudinal vortices at each rear end corners, as shown by Wong and Mair (1983) and Grandemange et al. (2015). We would like to point out that, although the Reynolds number of the present study is lower than typical values of the heavy vehicles under real flow conditions, it is sufficiently large to extrapolate our results to larger values of Re. In fact, our results are in very good agreement with those of Grandemange et al. (2015), at $Re = 2.5 \times 10^6$, in terms of the drag coefficient.

Finally, the overall fluctuating dynamics at the wake and the periodic vortex shedding mode are next analyzed for the three configurations with the help of Fig. 5, which depicts the PSD of the streamwise velocity fluctuations, $u'_x = u_x - U_x$, measured using a hot-wire anemometry (HWA) probe placed at $P_{\rm hwa} = (x, y, z) = (2.5, 0, 0.35)$ (see black point in inset of Fig. 5). The selected location of the hot-wire probe is outside of the recirculation region as the L_r values showed in Fig. 3 indicate. As observed, the spectrum of the reference wake is characterized by a dominant frequency, $St_z = 0.175$, which corresponds to the global vertical shedding mode emanating from the interaction between the upper and lower shear layers. This value is in good agreement with those reported by Grandemange et al. (2013b) and Lorite-Díez et al. (2019), and remains barely unaltered when the rear cavities are installed.

In general, the addition of a straight cavity induces only a slight weakening of the amplitude of the velocity fluctuations near the resonant frequency, indicating a less energetic shedding process at the measurement point. However, when the curved device is incorporated, an overall attenuation of the velocity fluctuations is achieved as shown in Fig 3(c).

All in all, the general attenuation of wake fluctuations and the limited size of the near wake render the curved cavity an efficient control device under conditions of flow aligned with the longitudinal axis of the body. Nevertheless, as it will be subsequently shown, such advantages become more evident under cross-wind conditions.

3.2. *Flow features under cross-wind conditions* ($\beta > 0$)

As it was discussed in Sect. 1, real vehicles are usually subject to cross-wind conditions that lead to resultant incident relative air velocities which are not aligned with the body. The wind incident angle, or yaw angle β (see Fig. 1), rarely exceeds the effective value of $10°$ (Hucho and Sovran, 1993). In particular, as detailed by

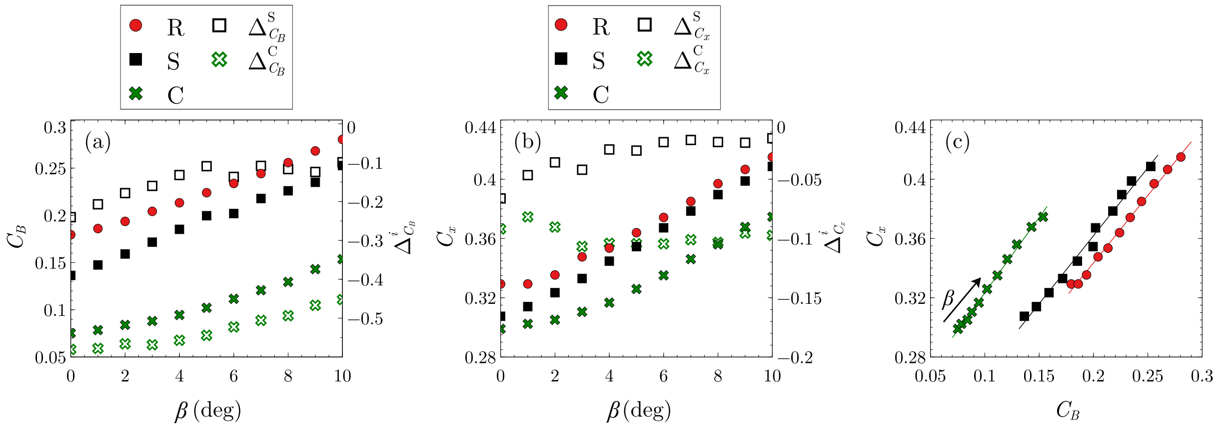

Figure 6: Mean base pressure and drag coefficient under cross-wind conditions for the three configurations studied. (a) Suction coefficient, C_B, and relative variations with respect to the reference case at each tested yaw angle, $\Delta^i_{C_B}$, versus β. (b) Body-axis mean drag coefficient, C_x, and relative variations with respect to the reference case at each tested yaw angle, $\Delta^i_{C_x}$, versus β. (c) Body-axis drag coefficient C_x against the suction coefficient C_B for increasing values of the yaw angle β. Filled (resp. hollow) symbols represent absolute (resp. relative) values in (a, b). The arrow in (c) indicates the increasing values of β, while solid lines represent linear fits of the experimental data.

D'Hooge et al. (2014); Garcia de la Cruz et al. (2017), the PDF of yaw angle experienced at 100-120 km/h is mostly defined by the interval $\beta < 12°$ (the range from zero to six degrees covering approximately 88% of the probability distribution shown in D'Hooge et al., 2014), and peaks around $\beta = 2°$. Thus, in view of such practical bounds, we decided to limit our study to $\beta \leq 10°$. That said, we will first analyze the effect of the yaw angle on the mean base pressure and force coefficients. Fig. 6(a) shows the evolution of C_B as β increases for the three different models considered in the present work, along with the relative variations with respect to the reference case, $\Delta^{\mathrm{S}}_{C_B}$ and $\Delta^{\mathrm{C}}_{C_B}$, respectively. As observed, for the three cases, C_B increases with β, although the absolute increase of C_B is higher for the reference case (model without a cavity) and for the model with a straight cavity, i.e. $(C^{\mathrm{R}}_B|_{\beta=10°} - C^{\mathrm{R}}_B|_{\beta=0°}) = 0.10$ and $(C^{\mathrm{S}}_B|_{\beta=10°} - C^{\mathrm{S}}_B|_{\beta=0°}) = 0.12$ while $(C^{\mathrm{C}}_B|_{\beta=10°} - C^{\mathrm{C}}_B|_{\beta=0°}) = 0.08$ for the curved cavity model. In fact, the value of $C^{\mathrm{C}}_B|_{\beta=10°}$ at $\beta = 10°$ for the curved cavity model is similar to that of $C^{\mathrm{S}}_B|_{\beta=0°}$ at $\beta = 0°$ for the straight cavity case and much smaller than $C^{\mathrm{R}}_B|_{\beta=0°}$ at $\beta = 0°$ for the reference model. Interestingly, suction reductions larger than 45% are achieved with the curved cavity even at large yaw angles. Smaller reductions are obtained with the straight cavity. Similarly, Fig. 6(b) displays that the drag coefficient in the body-axis frame of reference, C_x (note that the body and load cell turn jointly in the set-up), also increases with β. The figure shows that, with respect to C_x, the improved behavior of the straight cavity becomes negligible for $\beta \geq 6°$. On the contrary, the performance of the curved cavity gets even better as β increases, achieving drag reductions around 10%. Finally, Fig. 6(c) depicts the force coefficient C_x versus C_B for increasing values of the yaw angle β and the three geometries considered. As expected, both C_x and C_B are linearly correlated and increase with the yaw angle regardless of the model configuration. Furthermore, the reference and the straight cavity cases show nearly parallel trends. However, the efficiency of the straight cavity decreases as β increases, leading to smaller C_B reductions with respect to the reference case at larger values of β (see Fig. 6a), i.e. $\Delta^{\mathrm{S}}_{C_B}|_{\beta=0°} = -24.0\%$ versus $\Delta^{\mathrm{S}}_{C_B}|_{\beta=10°} = -9.6\%$.

On the other hand, the curved cavity body exhibits considerably lower values of both coefficients for the whole range of yaw angle investigated. Thus, it is a configuration more robust to cross-wind conditions than the other two, and especially with respect to the straight cavity. For example, note that at $\beta = 10°$ the drag coefficient values for the three configurations are $C^{\mathrm{R}}_x = 0.415$, $C^{\mathrm{S}}_x = 0.409$ and $C^{\mathrm{C}}_x = 0.375$, what represent relative reductions with respect to the reference case of $\Delta^{\mathrm{S}}_{C_x}|_{\beta=10°} = -1.4\%$ and $\Delta^{\mathrm{C}}_{C_x}|_{\beta=10°} = -9.6\%$ for the straight and curved cavities, respectively (see Fig. 6b). Thus, it is clear that the curved cavity represents an efficient drag reduction strategy under cross-wind conditions, while the straight cavity reduces dramatically its performance as β increases.

In the same line, the side force coefficient in the body frame of reference, C_y, increases with β more significantly for the reference case and straight cavity configuration than for the curved cavity, as shown in

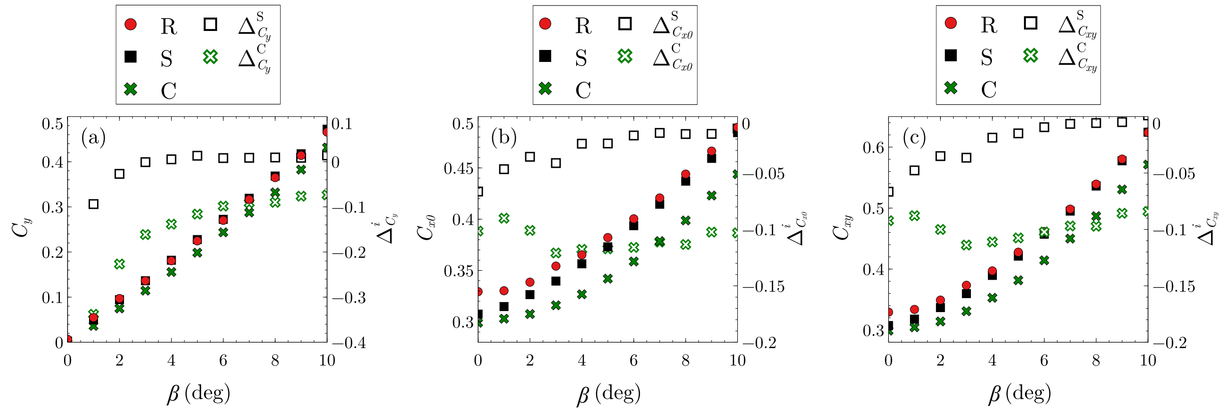

Figure 7: Lateral forces evolution under cross-wind conditions for the three employed configurations. (a) Mean side coefficient, C_y, and relative variations with respect to the reference case at each tested yaw angle, $\Delta^i_{C_y}$, versus β. (b) Total horizontal force coefficient, C_{xy}, and relative variations with respect to the reference case at each tested yaw angle, $\Delta^i_{C_{xy}}$, versus β. (c) Mean drag coefficient in the wind direction, C_{x0} given by Eq. (5), and relative variations with respect to the reference case at each tested yaw angle, $\Delta^i_{C_{x0}}$, versus β. Filled (resp. hollow) symbols represent absolute (resp. relative) values.

Fig. 7 (a). Note that, in this case, the lateral areas of the bodies with the straight and curved cavities are bigger, since their lengths are increased when the cavities are added, contributing to increase the lateral force, f_y.

Thus, although the straight cavity can contribute to reducing the lateral force, the effect of the increased area makes the side force even greater than that of the reference body for $\beta > 3°$. However, C_y^{C} behaves differently for the curved geometry, giving values of the side force even smaller than the body without cavity, what suggests a better interaction with the non-aligned incoming flow. This behaviour translates into a significant reduction of the lateral force compared to the reference case, as the yaw angle increases, $\Delta^{\mathrm{C}}_{C_y}|_{\beta=10°} = -7.5\%$, while the straight cavity produces the opposite effect, leading to the increase of the force, with $\Delta^{\mathrm{C}}_{C_y}|_{\beta=10°} = 1.5\%$.

Furthermore, the combined effect of the yaw angle for the different configurations is obtained by computing the total horizontal force coefficient, $C_{xy} = \sqrt{C_x^2 + C_y^2}$, i.e. the magnitude of the horizontal force acting on the body, equal to the composition between the local-axes drag and side forces, which increases quadratically with β but at different rate, depending on the tested configurations. In that sense, Fig. 7(b) depicts the evolution with the yaw angle of both the coefficient C_{xy} and the corresponding relative variation with respect to the reference case, $\Delta^i_{C_{xy}}$, for the straight and curved cavities. In particular, the straight device shows that its performance gets worse as β increases, achieving values of C^{S}_{xy} nearly equal to those obtained in the reference body for $\beta > 6°$, with $\Delta^{\mathrm{S}}_{C_{xy}}|_{\beta=10°} \simeq 0$. However, the use of the curved device (with the same total length as the straight cavity configuration) displays reductions in C_{xy} of at least 8% over the whole range of β, indicating a lower total aerodynamic resistance to different flow conditions, what is important in terms of driving stability and fuel consumption. Such advantage is also clearly evidenced if the drag coefficient in the wind direction, C_{x_0} (see Eq. 5), is considered, as Fig. 7(c) shows. As observed, the straight device displays a faster quadratic increase of C_{x_0} such that, for $\beta \gtrsim 6°$, the values of the drag coefficient nearly match those of the reference model, being the relative reduction of drag coefficient $\Delta^S_{C_{x_0}} \simeq 1\%$ at $\beta = 10°$ (Fig. 7c). Conversely, the curved cavity provides drag reductions of about 10% for the whole range of yaw angle investigated, as Fig. 7(c) shows.

The near wake topology and base pressure distribution will be next analyzed using PIV and pressure measurements in order to understand the mechanisms leading to the differences observed in the force and pressure coefficients among the tested configurations. The near wake structure is displayed in Fig. 8 in a global coordinate frame, through time-averaged contours of the spanwise vorticity, Ω_z, and flow streamlines, for the three configurations in the horizontal plane $z = 0$, at three different yaw angles. The wake behind the reference square-back body at $\beta = 0°$ shows a nearly symmetric recirculating bubble (due to the contribution of both equally probable asymmetric P and N states) with two counter-rotating eddies, which are associated

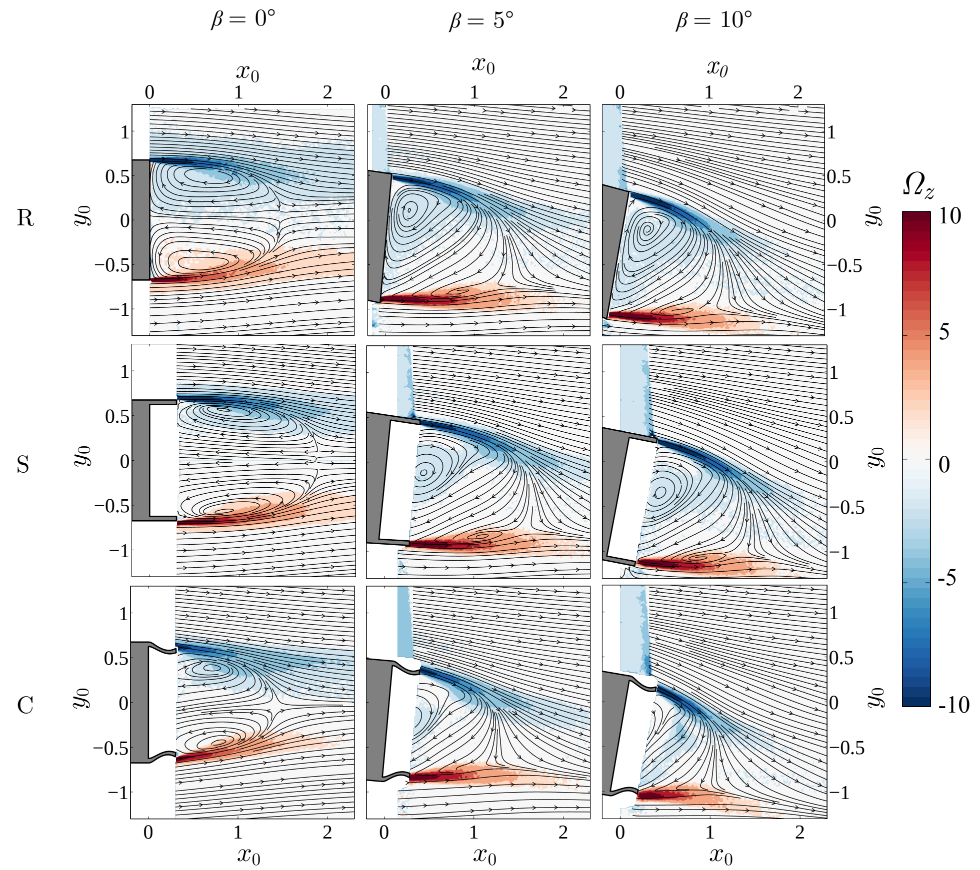

Figure 8: Contours of time-averaged spanwise vorticity, Ω_z, and corresponding flow streamlines at selected yaw angles, $\beta = 0°, 5°$ and $10°$, for the three configurations under study.

with moderate values of the vorticity compared to the higher value of Ω_z at the shear layers, and regions of minimum pressure within the vortex cores.

When the body is slightly yawed (e.g. $\beta \geq 0.5^{o}$), the wake loses the bi-stable behavior, since this phenomenon is very sensitive to misalignments between the body axis and the incoming flow and thus, one of the RSB states is fixed at the wake. As observed for $\beta = 5°$ and $10°$, the body misalignment induces the deflection of the recirculation bubble towards the leeward side, displaying a single vortex whose size increases with β. The vortex core is progressively displaced toward the base of the body as β grows, a phenomenon associated with the base pressure decrease. As far as the model with straight cavity is concerned, a similar modification process of the recirculation bubble is observed as β increases. The initial symmetric elliptical recirculating region gives rise to a single deflected clockwise vortex core under cross-wind conditions. However, in this case the attached vortex is smaller than in the reference case and is located further downstream from the body base, contributing to the increase of the base pressure and thus to the decrease of the base pressure coefficient, as shown in Fig. 6(a). Finally, the near-wake behind the model with curved cavity displays the smallest vortex with low recirculating velocities and vorticity. In spite of the higher curvature of flow streamlines, which may induce larger base suction according to Roshko (1993), the extension of the deflected clockwise vortex core developed under an increasing yawed incident flow is very limited by the span between the rear edges of the cavity. Thus, although such vortex may enter the cavity, its contribution as source of low pressure is considerably attenuated, as seen in Fig. 6(a).

In general, starting from nearly symmetric shapes at $\beta = 0°$, the recirculating bubbles are shown to deflect in the direction of the cross-wind for $\beta \neq 0°$, and become progressively shorter as β grows. Such trends are clearly observed in Fig. 9(a), where the time-averaged recirculation region length, L_r, is represented as a function of β. As observed, the value of L_r decreases monotonously with the yaw angle for the three

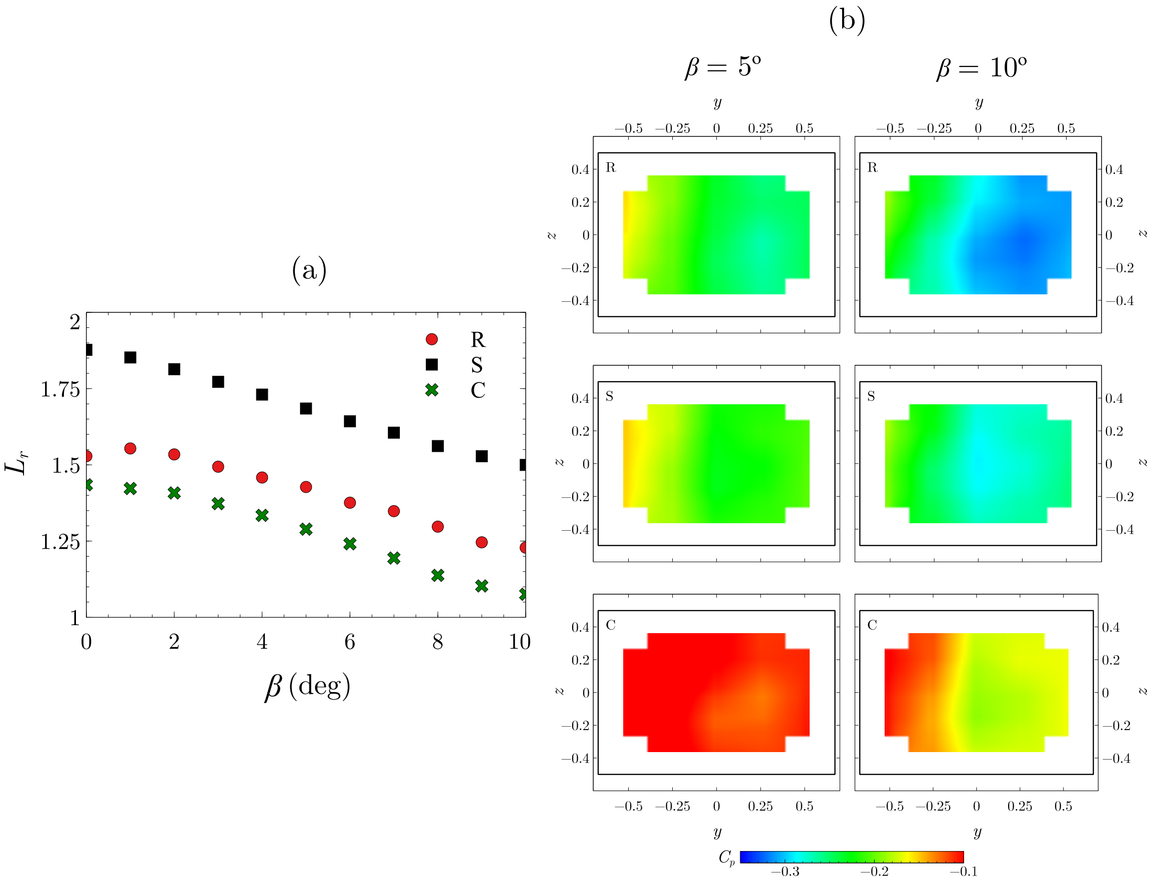

Figure 9: (a) Evolution of the recirculation region length, L_r, versus yaw angle β for the three tested geometries. Averaged contours of pressure C_p at selected yaw angles, 5° and 10°, for the three configurations under study.

configurations, being always $L_r^{\mathrm{S}} > L_r^{\mathrm{R}} > L_r^{\mathrm{C}}$, regardless of the yaw angle. Interestingly, the shortening of the recirculation bubble follows a nearly linear trend for the straight cavity case, with important differences between values at $\beta = 0°$ and 10°, indicating a large impact of the flow misalignment on the near wake. For the curved device, the relative decrease of L_r is similar, but quadratic, thus featuring minimum changes under cross-wind conditions for small values of β. Moreover, as observed in Fig. 8, the recirculating bubble is less deflected by the increasing yaw angles while its corresponding width remains limited by the cavity edges, and therefore, the impact on the base pressure decrease is less acute. Such effect can be also observed in the pressure distribution measured on the base of the body for $\beta = 5^{\circ}$ and 10° (see Fig. 9b). For both yaw angles, a clear asymmetry in the pressure distribution exists, resulting into important low pressure regions in the windward side of the base. The level of such low pressure region is reduced when yaw is increased. However, the base pressure inside the cavity hollow is considerably less negative for the curved device than for the straight one, in agreement with the trends presented in Figs. 6 and 7.

4. Conclusions

The performance of straight and curved cavities as passive control devices at the base of a square-back Ahmed body, has been experimentally evaluated at $Re = 1 \times 10^5$, under cross-wind conditions, by means of pressure, force and PIV measurements. The design of the curved device constitutes a three-dimensional adaptation of the shape obtained by Lorite-Díez et al. (2017) using adjoint sensitivity and shape optimization techniques, for two-dimensional wakes. The comparative study based on the evaluation of force and pressure coefficients and the description of the near wake topology, has been performed considering the reference square-back body (without any passive control device), and bodies implementing a straight cavity and a curved one of same depth and thickness ($d/h = 0.3$ and $t/h = 0.05$ respectively, with h being the model's height). Both passive devices have been implemented as add-on parts, thus increasing the reference model's length, as would occur in practical heavy vehicles applications where devices are appended to the base.

In general, the body with the curved cavity has been shown to be more robust and efficient than the classical straight cavity in terms of wake control and drag reduction, especially under cross-wind conditions, where the performance of a straight cavity is considerably hindered. In particular, for an incident freestream aligned with the body, both devices have been shown to efficiently attenuate the bi-stable dynamics in the horizontal axis, characterized by the switching between the two mirror asymmetric P (positive) and N (negative) modes, although the curved cavity improves the total wake asymmetry. The reduced size of the near wake induced by such device, which is limited by the span between the rear edges of the cavity, modifies the structure of the recirculating region, reducing the intensity of the vorticity and increasing the base pressure. Thus, the base pressure recovery translates into relative reductions of drag and suction coefficients of $\Delta^{\mathrm{C}}_{C_x}|_{\beta=0^\circ} = -9.1\%$ and $\Delta^{\mathrm{C}}_{C_B}|_{\beta=0^\circ} = -58.1\%$ with respect to the reference case. Regarding the periodic vortex shedding mode, the amplitude of fluctuations are more efficiently attenuated by the curved cavity, due to a reduced spanwise extension of the wake, and a more regular shedding process as in the two-dimensional wake analyzed by Lorite-Díez et al. (2017).

More importantly, the effect of cross-wind has been also evaluated by modifying the yaw angle. Interestingly, in spite of the common trends for the three configurations, characterized by an increase of the force coefficients with the yaw angle, the corresponding variations are smaller for the model with the curved cavity, which appears as a more robust device under cross-wind. In particular, the relative reduction of drag coefficient (in the wind direction) provided by the straight cavity with respect to the reference squareback model falls up to a value of $\Delta^{\mathrm{S}}_{C_x} = -1.4\%$ at $\beta = 10^\circ$, whereas the curved device provides $\Delta^{\mathrm{C}}_{C_x} \approx -9\%$ within the whole range of yaw angle investigated. Such dramatic decrease on the performance of the straight cavity (which had not been previously discussed in depth in the literature) stems partially from the considerable decrease of the recirculation region as the wake is deflected when the incident flow is yawed. Additionally, the leeward clockwise vortex core formed at the corresponding near wake is wider than that observed for the curved cavity, whose size is limited by the span of the rear edges and, consequently, its contribution as a source of low pressure is also reduced.

All in all, it has been shown that a straight cavity does not necessarily constitute an efficient control strategy under cross-wind conditions, especially when compared with a curved cavity. Moreover, the suitability of simplified two-dimensional adjoint optimization approaches to design efficient flow control strategies has been satisfactorily proven for a three-dimensional turbulent wake implementing a rear curved cavity. Nonetheless, the use of such device should be further tested at industrial scale to confirm the reported trends and results prior to application in real vehicles, and compared with other passive control techniques, i.e. boat tailing or slanted flaps. Interestingly, as mentioned earlier, the slant angle of the curved cavity obtained by means of the optimization study was 12.5°, which is similar to the optimal orientation given for rear flaps in previous studies (see e.g. Khalighi et al., 2012; Grandemange et al., 2015; Hoffmann et al., 2015; Garcia de la Cruz et al., 2017; Schmidt et al., 2018). In that sense, although a slanted cavity may behave better than a straight cavity under cross-wind conditions, a longer slanted cavity might be required to obtain similar results. This idea is supported by the numerical simulations performed in the optimization study by (Lorite-Díez et al., 2017), where it is discussed how the outer concave profile of the cavity induces a longitudinal adverse pressure gradient which decelerates the flow, and deflects it inwards, generating a recirculating region thinner than that of a straight geometry or intermediate (less curved) slanted geometries. However, a general comparison with other passive devices was out of the scope of the present work, conceived as a experimental validation study of the previously reported two-dimensional results.

Nevertheless, controlled experiments performed in a wind-tunnel do not reproduce real flow conditions, where transient effects and gusts, among others, are not considered. Moreover, the effect of the Reynolds number is also worth investigating, although the present value of $Re = 10^5$ can be considered sufficiently large to provide useful measurements for applications that can be extrapolated to more realistic conditions. Anyway, we are currently planning a series of experimental campaigns to compare the performance of real trucks with and without the curved cavity in a racing circuit, as well as on the highway, and therefore corroborates the results provided herein.

Acknowledgements

This work has been partially supported by the Spanish MINECO and European Funds under projects DPI2017-89746-R and DPI2017-88201-C3-2-R. Moreover, J.I.J.G. and M.L.D want to thank the Spanish MECD for the financial support provided, respectively, under José Castillejo grant CAS18/00379 and Fellowship FPU 014/02945.

References

Acker, A., 2018. Key Transport Statistics 2018. Technical Report. International Transport Forum.

Ahmed, S.R., Ramm, G., Faltin, G., 1984. Some salient features of the time-averaged ground vehicle wake. SAE Technical Paper 840300.

Bello-Millán, F., Makela, T., Parras, L., del Pino, C., Ferrera, C., 2016. Experimental study on Ahmed's body drag coefficient for different yaw angles. Journal of Wind Engineering and Industrial Aerodynamics 157, 140–144.

Bonnavion, G., Cadot, O., 2018. Unstable wake dynamics of rectangular flat-backed bluff bodies with inclination and ground proximity. Journal of Fluid Mechanics 854, 196–232.

Brackston, R.D., García de la Cruz, J.M., A., W., Rigas, G., Morrison, J.F., 2016. Stochastic modelling and feedback control of bistability in a turbulent bluff body wake. Journal of Fluid Mechanics 802, 726–749.

Choi, H., Lee, J., Park, H., 2014. Aerodynamics of heavy vehicles. Annual Review of Fluid Mechanics 46, 441–468.

García de la Cruz, J., Oxlade, A., Morrison, J., 2017. Passive control of base pressure on an axisymmetric blunt body using a perimetric slit. Physical Review Fluids 2, 043905.

D'Hooge, A., Palin, R., Rebbeck, L., Gargoloff, J., Duncan, B., 2014. Alternative simulation methods for assessing aerodynamic drag in realistic crosswind. SAE International Journal of Passenger Cars-Mechanical Systems 7, 617–625.

Evrard, A., Cadot, O., Herbert, V., Ricot, D., Vigneron, R., Délery, J., 2016. Fluid force and symmetry breaking modes of a 3D bluff body with a base cavity. Journal of Fluids and Structures 61, 99–114.

Garcia de la Cruz, J., Brackston, R.D., Morrison, J.F., 2017. Adaptive base-flaps under variable cross-wind, in: SAE Technical Paper, SAE International.

Gardell, L., 1980. Low Drag Truck Cabs. Technical Report. SacaniaDiv. Saab-Scania.

Grandemange, M., Cadot, O., Courbois, A., Herbert, V., Ricot, D., Ruiz, T., Vigneron, R., 2015. A study of wake effects on the drag of Ahmed's squareback model at the industrial scale. Journal of Wind Engineering and Industrial Aerodynamics 145, 282–291.

Grandemange, M., Cadot, O., Gohlke, M., 2012. Reflectional symmetry breaking of the separated flow over three-dimensional bluff bodies. Physical review E 86, 035302.

Grandemange, M., Gohlke, M., Cadot, O., 2013a. Bi-stability in the turbulent wake past parallelepiped bodies with various aspect ratios and wall effects. Physics of Fluids 25, 095103.

Grandemange, M., Gohlke, M., Cadot, O., 2013b. Turbulent wake past a three-dimensional blunt body. Part 1. Global modes and bi-stability. Journal of Fluid Mechanics 722, 51–84.

Han, T., Sumantran, V., Harris, C., Kuzmanov, T., Huebler, M., Zak, T., 1996. Flow-field simulations of three simplified vehicle shapes and comparisons with experimental measurements. SAE Technical Paper 960678.

Hassaan, M., Badlani, D., Nazarinia, M., 2018. On the effect of boat-tails on a simplified heavy vehicle geometry under crosswinds. Journal of Wind Engineering and Industrial Aerodynamics 183, 172–186.

Hoffmann, F., Schmidt, H.J., Nayeri, C., Paschereit, O., 2015. Drag reduction using base flaps combined with vortex generators and fluidic oscillators on a bluff body. SAE Int. J. Commer. Veh. 8, 705–712.

Hucho, W., Sovran, G., 1993. Aerodynamics of road vehicles. Annual Review of Fluid Mechanics 25, 485–537.

Khalighi, B., Chen, K.H., Iaccarino, G., 2012. Unsteady aerodynamic flow investigation around a simplified square-back road vehicle with drag reduction devices. Journal of Fluids Engineering 134, 061101.

Li, R., Borée, J., Noack, B.R., Cordier, L., Harambat, F., 2019. Drag reduction mechanisms of a car model at moderate yaw by bi-frequency forcing. Physical Review Fluids 4, 034604.

Lorite-Díez, M., Jiménez-González, J., Gutiérrez-Montes, C., Martínez-Bazán, C., 2017. Drag reduction of slender blunt-based bodies using optimized rear cavities. Journal of Fluids and Structures 74, 158–177.

Lorite-Díez, M., Jiménez-González, J.I., Gutiérrez-Montes, C., Martínez-Bazán, C., 2018. Effects of rear cavities on the wake behind an accelerating d-shaped bluff body. Physics of Fluids 30, 044103.

Lorite-Díez, M., Jiménez-González, J.I., Pastur, L., Martínez-Bazán, C., Cadot, O., 2019. Experimental analysis on the effect of local base blowing on three-dimensional wake modes. Journal of Fluid Mechanics .

Martín-Alcántara, A., Sanmiguel-Rojas, E., Gutiérrez-Montes, C., Martínez-Bazán, C., 2014. Drag reduction induced by the addition of a multi-cavity at the base of a bluff body. Journal of Fluids and Structures 48, 347–361.

McArthur, D., Burton, D., Thompson, M., Sheridan, J., 2018. An experimental characterisation of the wake of a detailed heavy vehicle in cross-wind. Journal of Wind Engineering and Industrial Aerodynamics 175, 364–375.

Meliga, P., Boujo, E., Pujals, G., Gallaire, F., 2014. Sensitivity of aerodynamic forces in laminar and turbulent flow past a square cylinder. Physics of Fluids (1994-present) 26, 104101.

Othmer, C., 2014. Adjoint methods for car aerodynamics. Journal of Mathematics in Industry 4, 1–23.

Rao, A., Minelli, G., Basara, B., Krajnović, S., 2018. On the two flow states in the wake of a hatchback ahmed body. Journal of Wind Engineering and Industrial Aerodynamics 173, 262–278.

Roshko, A., 1993. Perspectives on bluff body aerodynamics. Journal of Wind Engineering and Industrial Aerodynamics 49, 79 – 100.
Sanmiguel-Rojas, E., Jiménez-González, J.I., Bohorquez, P., Pawlak, G., Martínez-Bazán, C., 2011. Effect of base cavities on the stability of the wake behind slender blunt-based axisymmetric bodies. Physics of Fluids (1994-present) 23, 114103.
Schmidt, H.J., Woszidlo, R., Nayeri, C.N., Paschereit, O., 2018. The effect of flow control on the wake dynamics of a rectangular bluff body in ground proximity. Experiments in Fluids 59, 107.
Wong, D., Mair, W., 1983. Boat-tailed afterbodies of square section as drag-reduction devices. Journal of Wind Engineering and Industrial Aerodynamics 12, 229–235.
Wood, R.M., Bauer, S.X., 2003. Simple and low-cost aerodynamic drag reduction devices for tractor-trailer trucks. SAE Transactions , 143–160.